Model for ferromagnetic Weyl and nodal line semimetals: Topological invariants, surface states, anomalous and spin Hall effect

Tomáš Rauch,[1,*] Huong Nguyen Minh,[1] Jürgen Henk,[1] and Ingrid Mertig[1,2]
[1]*Institute of Physics, Martin Luther University Halle-Wittenberg, Halle (Saale), Germany*
[2]*Max Planck Institute for Microstructure Physics, Halle (Saale), Germany*
(Received 4 October 2017; published 4 December 2017)

A model based on the Dirac equation allows one to describe topological insulators. In this paper we extend this model by adding a Zeeman term to introduce magnetism. By this means we show that it can be used to describe the electronic properties of ferromagnetic Weyl and nodal line semimetals, which arise for distinct parameters of the model. We confirm the topological nontriviality of the nodal objects by calculating the topological invariants, as well as by demonstrating the existence of topological surface states in the spectral function of the semi-infinite systems. Furthermore, we calculate the anomalous and spin Hall conductivities for various model parameters, which allows us to identify typical signatures of Weyl points and nodal lines in electronic transport.

DOI: 10.1103/PhysRevB.96.235103

I. INTRODUCTION

Topological properties of materials are one of the key topics of solid-state physics discussed in the last decade. After the initial discoveries of two-dimensional (2D) [1,2] and three-dimensional (3D) topological insulators (TIs) [3], the focus of the community turned also toward metallic nontrivial materials. Dirac semimetals [4–8], Weyl semimetals (WSMs) [9–12], nodal line semimetals (NLSMs) [13–18], and other semimetals with even more exotic low-energy excitations [19] are studied with increasing effort in recent years.

A typical manifestation of the properties of topological insulators are the quantum anomalous Hall effect (QAHE) [20,21] in the case of broken time-reversal symmetry and the quantized spin Hall effect (QSHE) [22–24] when the time-reversal symmetry is preserved. The QSHE is a variant of the spin Hall effect (SHE) [25,26] which shows a constant spin Hall conductivity (SHC) if the Fermi energy (E_F) is located in the insulating band gap. The SHC in trivial and topological insulating systems was recently calculated in Ref. [27]. If E_F is not located in the band gap, which is necessarily the case in metals and semimetals, then the anomalous and spin Hall conductivities show no quantization and change with varying E_F (e.g., by doping). Therefore, to observe both anomalous Hall effect (AHE) and SHE in WSMs and NLSMs, two ingredients are necessary: magnetic order (to break time-reversal symmetry) and spin-orbit coupling (SOC). It has been shown earlier that the Weyl points (WPs)—band touching points in a WSM—always exist in pairs [28] and the anomalous Hall conductivity (AHC) for E_F at the WP energy is proportional to their distance in the reciprocal space [29,30]. This behavior can be straightforwardly extended to the SHC by assuming that the anomalous Hall current is spin polarized [31].

In the case of NLSMs the situation is more complicated than for the WSMs. Usually, two types of NLSMs are discussed; type 1 protected by mirror symmetry with the nodal loop located in a mirror plane of the Brillouin zone (BZ) and type 2 with inversion and time-reversal symmetries being present but in absence of SOC [32]. Because we study the AHE and SHE in ferromagnetic NLSMs, we have to restrict ourselves to type 1. Generally, NLSMs of Dirac type (fourfold degenerate nodal line) and of Weyl type (twofold degenerate nodal line) are possible. In the case of broken time-reversal symmetry we will only observe nodal lines of the Weyl type. Weyl nodal lines of type 1 were already demonstrated to exist in $PbTaSe_2$ [16] and $TlTaSe_2$ [33], which are nonmagnetic but lack inversion symmetry. Even earlier, this type of nodal lines coexisting with WPs was predicted from *ab initio* to exist in ferromagnetic $HgCr_2Se_4$ [34]. Recently, other ferromagnetic materials, CrO_2 [35] and half-metallic Heusler Co_2TiX (X = Se, Ge, or Sn) [36], were predicted to host nodal lines (NLs).

In this paper we adopt a model based on the extended Dirac equation [37] previously used to describe TIs in two and three dimensions. We further manipulate this model in order to study the influence of ferromagnetism on the electronic bands of insulators and to show that such a system can undergo a phase transition from an insulating phase to a WSM or a NLSM. In addition, we calculate the AHC and SHC for different topological phases described by the model and thus identify the main contributions of the semimetallic features to the spin and electronic transport. Our findings thus complement the results obtained for topological semimetals in realistic [38] and model [39] systems featuring antiferromagnetic and noncollinear magnetic order as well as in nonmagnetic materials [31].

This paper is organized as follows. In Sec. II we will introduce the model Hamiltonian and demonstrate the existence of WSM and NLSM phases for distinct parameter values. We will proof the nontrivial topology by calculating topological invariants and compare the results with surface electronic structure calculations for a semi-infinite geometry. In Sec. III we will calculate the AHC and SHC for the different systems and discuss the effect of WPs and NLs on these transport quantities. In Sec. IV we will suggest ferromagnetic materials, in which WPs and NLs could exist. Finally, we will give a conclusion in Sec. V.

II. TOPOLOGICAL PROPERTIES

A. Model Hamiltonian

The basis of the model we use in this paper is the Dirac equation of a free particle [40],

$$H = c\vec{p}\cdot\vec{\alpha} + mc^2\beta. \tag{1}$$

*Corresponding author: tomas.rauch@physik.uni-halle.de

c is the velocity, $\vec{p}$ the momentum, $\vec{\alpha}$ and β the 4×4 Dirac matrices, and m the mass, which take on the role of model parameters when the equation is used to describe electrons and holes in a solid near the fundamental band gap governed by the mass m. In order to describe TIs [37], Eq. (1) has to be extended by $Mp^2\beta$. This term is the lowest term in the p expansion of the potential which does not break the time-reversal symmetry. The 3D model then describes strong TIs for $m \cdot M > 0$ and trivial insulators for $m \cdot M < 0$.

In this paper, we additionally introduce a Zeeman term $\beta\vec{\Sigma} \cdot \vec{B}$ with $\vec{\Sigma}$ the relativistic spin operator and $\vec{B}$ an exchange field, either induced by magnetization or applied externally. This term breaks the time-reversal symmetry and induces an exchange splitting of the Kramers degenerate bands, which may lead to the existence of WSMs and NLSMs. Thus, we end up with the model Hamiltonian

$$H = c\vec{p} \cdot \vec{\alpha} + (mc^2 - Mp^2)\beta + \beta\vec{\Sigma} \cdot \vec{B}. \tag{2}$$

Note that a similar Hamiltonian was introduced in Ref. [13]. Recently, Yu *et al.* [39] studied a related model for antiferromagnetic half-Heusler materials, which also features various topological phases.

For further calculations of topological invariants in a finite BZ and to be able to consider a slab or semi-infinite geometry, we make the Hamiltonian (2) periodic on a cubic lattice (lattice constant a) by substituting

$$\begin{aligned} p_\alpha &\to \frac{\hbar}{a}\sin(ap_\alpha/\hbar) \\ p_\alpha^2 &\to \frac{2\hbar^2}{a^2}[1 - \cos(ap_\alpha/\hbar)] \end{aligned} \qquad \text{with } \alpha = x,y,z, \tag{3}$$

similar to Refs. [37,41]. The Hamiltonian then becomes

$$H = m_0c^2\begin{pmatrix} m - 2MK(\vec{p}) + B & 0 & c\,\sin(p_z) & c[\sin(p_x) - i\,\sin(p_y)] \\ 0 & m - 2MK(\vec{p}) - B & c[\sin(p_x) + i\sin(p_y)] & -c\,\sin(p_z) \\ c\,\sin(p_z) & c[\sin(p_x) - \mathrm{i}\sin(p_y)] & -m + 2MK(\vec{p}) - B & 0 \\ c[\sin(p_x) + i\,\sin(p_y)] & -c\,\sin(p_z) & 0 & -m + 2MK(\vec{p}) + B \end{pmatrix} \tag{4}$$

by introducing the rest mass m_0c^2 and redefining the parameters as $m/m_0 \to m$, $M\hbar^2/(a^2m_0c^2) \to M$, $c\hbar/(am_0c^2) \to c$, $\vec{B}/(m_0c^2) \to \vec{B}$, $p_\alpha a/\hbar \to p_\alpha$, and with the abbreviation $K(\vec{p}) = 3 - \cos(p_x) - \cos(p_y) - \cos(p_z)$. We chose $\vec{B} = B\vec{e}_z$. Thus, m, M, c, $\vec{B}$, and $\vec{p}$ are dimensionless and m_0c^2 defines the energy scale of the model.

In real space, the Hamiltonian has the tight-binding form

$$\begin{aligned} H = m_0c^2 \sum_{i,j,k} &[\Gamma_0 c^\dagger_{i,j,k}c_{i,j,k} + \{\Gamma_x c^\dagger_{i+1,j,k}c_{i,j,k} \\ &+ \Gamma_y c^\dagger_{i,j+1,k}c_{i,j,k} + \Gamma_z c^\dagger_{i,j,k+1}c_{i,j,k} + \text{H.c.}\}] \end{aligned} \tag{5}$$

with matrix-valued on-site energy

$$\Gamma_0 = (m - 6M)\tau_0 \otimes \sigma_z + B\tau_z \otimes \sigma_z \tag{6}$$

and hopping amplitudes

$$\Gamma_\alpha = M\tau_0 \otimes \sigma_z - i\frac{c}{2}\tau_\alpha \otimes \sigma_x, \quad \alpha = x,y,z. \tag{7}$$

τ_α and σ_α, with $\alpha = x,y,z$, are the 2×2 Pauli matrices and τ_0 and σ_0 are the identity matrices. Equation (5) is particularly useful for description of semi-infinite systems.

B. Bulk topology

At this point, we investigate the WSM and NLSM phases which can emerge from the Hamiltonian (4). If not stated otherwise, in all following examples we will set $c = M = 1$ and $m = \pm 1$. We choose $m_0c^2 = 1\,\text{eV}$, which is the typical energy scale in insulators. Setting the exchange field $B = 0$ leads to two possible initial systems; a normal insulator for $mM < 0$ and a strong topological insulator (STI) for $mM > 0$ (Ref. [37]). The respective band structures are shown in Figs. 1(a) and 1(d). The normal insulator [Fig. 1(a)] has a parabolic dispersion at the Γ point, whereas in the STI case [Fig. 1(d)], the typical camel-back shape indicating the band inversion is clearly visible. Note that for $B = 0$ the bands are doubly degenerate because of the presence of both time-reversal and inversion symmetries.

Increasing the exchange field to finite values breaks the time-reversal symmetry and splits the Kramers degeneracy [see Figs. 1(b) and 1(e) for $B = 0.5$]. A first important semimetallic feature emerges immediately for nonvanishing exchange field. For $m = +1$ (i.e., the STI case) there are band crossings between the lowest two bands and between the highest two bands, respectively. The crossings are located along the Z-Γ-Z line in the BZ, which is parallel to the direction of the exchange field. We confirm that the crossings are Weyl points by calculating the Chern number of a sphere in $\vec{p}$ space surrounding a single crossing. The Chern number is calculated as [42–45]

$$C = \frac{1}{2\pi}\sum_n \int_S d^2p[\vec{\Omega}_n(\vec{p}) \cdot \vec{n}(\vec{p})]. \tag{8}$$

The sum is over all bands n up to the WP energy, S is the surface of a sphere, $\vec{\Omega}_n(\vec{p})$ is the Berry curvature, and $\vec{n}(\vec{p})$ is a unit vector perpendicular to the surface S. We obtain $C = \pm 1$ for all crossings, both the ones between bands 1 and 2, as well as those between bands 3 and 4, indicating that they are all WPs. Interestingly, the existence of WPs is here the consequence of band inversion together with the exchange field. No WPs emerge in the normal insulator case $m = -1$ [Fig. 1(b)].

Further increase of the exchange field leads to the overlap of the higher valence band with the lower conduction band (assuming $E_F = 0$). For the trivial insulator, the bands touch at the Γ point for $B = 1.0$. For higher exchange fields, a flat NL occurs at $E = 0.0\,\text{eV}$ in the $p_z = 0$ plane [Fig. 1(c)]. In the case of the TI, multiple NLSM phases occur upon increasing the exchange field (see Fig. 2). Because of the camel-back shape of

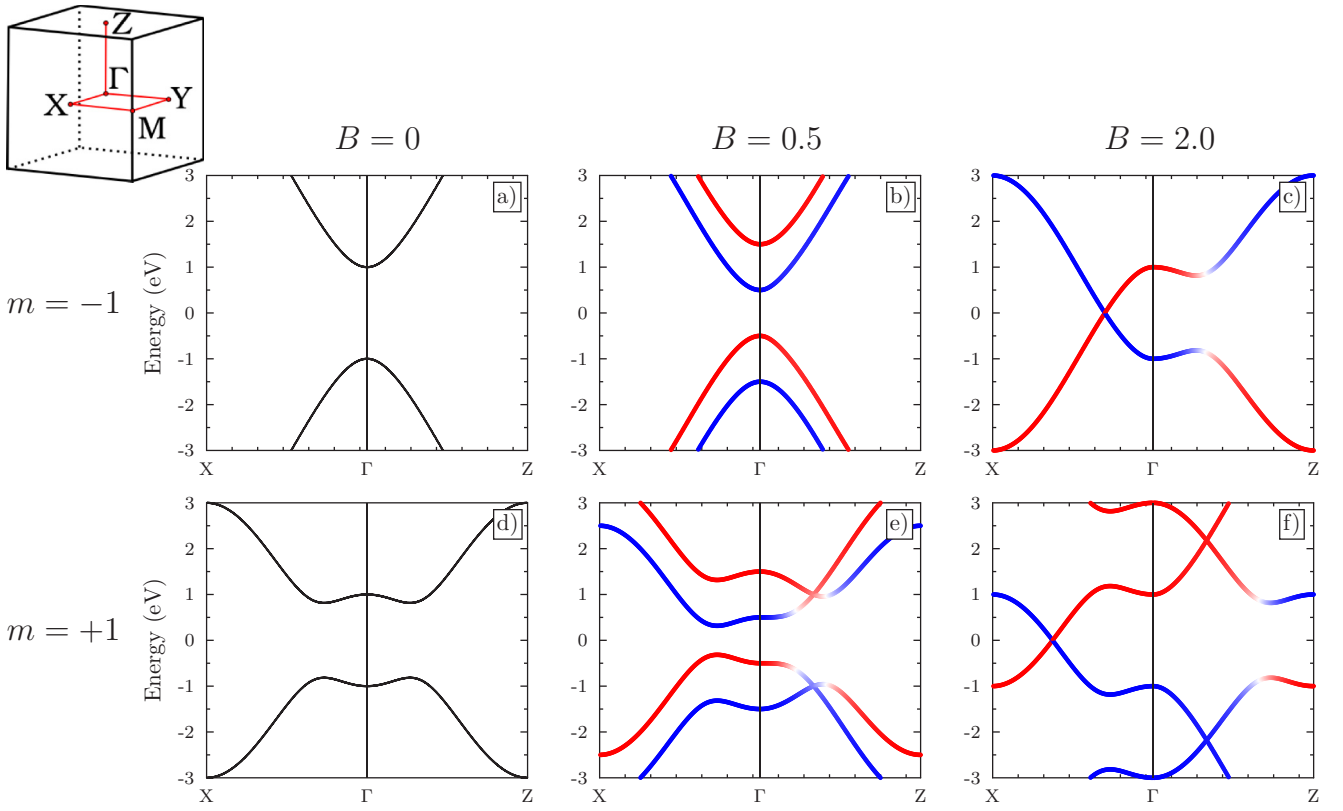

FIG. 1. Band structure of the Hamiltonian (4) for $m = -1$ [(a)–(c)] and $m = +1$ [(d)–(f)] for selected exchange fields: $B = 0$ [(a),(d)], $B = 0.5$ [(b),(e)], and $B = 2.0$ [(c),(f)]. The colors represent the value of the spin polarization (red: 1; blue: -1) along the z axis (parallel to $\vec{B}$). Inset: BZ of the cubic lattice.

the bands, the direct band gap of the insulating phase is located at the Γ-X line, off the Γ point. At this point the band gap closes for the first critical exchange field $B_c^1 \approx 0.8165$. Because of the C_4 rotational symmetry preserved in the magnetic system, four NLs emerge. A second phase transition happens at $B_c^2 \approx 0.845$, where the band gap closes also along the Γ-M line. The result is a pair of NLs, concentric around Γ. Note that in the case of the isotropic Hamiltonian (2) both Γ-M and Γ-X lines are equivalent and only the double-NL phase can exist. Finally, at $B_c^3 = 1.0$ the band gap closes also at Γ, the inner NL of the former pair vanishes, and only one NL remains [see Fig. 1(f)], similar to the trivial insulator. All NLs are protected by the mirror symmetry, which is preserved in the $p_z = 0$ plane because $\vec{B}$ is oriented along the z axis. In a mirror plane, the spin is oriented perpendicular to it and remains unchanged under the action of the mirror operator. Therefore, the z component of the spin operator commutes with the mirror operator and they share common eigenfunctions. A crossing of two bands with different mirror or spin eigenvalues [as indicated by red and blue in Fig. 3(a)] is allowed in the mirror plane, since the states do not hybridize with each other [32].

In addition to the mirror eigenvalues, the NLs in the Hamiltonian (4) are also protected by a Berry phase θ of a closed loop $\mathcal{L}$ piercing the NL [32,46]:

$$\theta(\mathcal{L}) = \sum_{n \in \text{occ.}} i \oint_{\mathcal{L}} \langle u_{n,\vec{p}} \| \nabla_{\vec{p}}\, u_{n,\vec{p}} \rangle d\vec{p}. \tag{9}$$

The integrand, $i\langle u_{n,\vec{p}} | \nabla_{\vec{p}}\, u_{n,\vec{p}} \rangle$, is the Berry connection. Owing to the presence of the mirror symmetry, the Berry phases θ

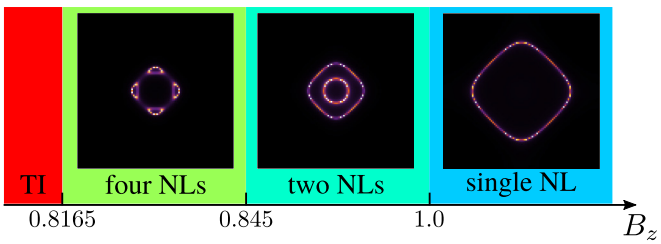

FIG. 2. Topological phases upon increasing B_z for $m = +1$. Displayed is the location of the NLs in the $p_z = 0$ plane.

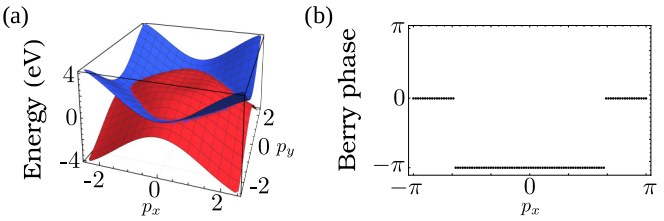

FIG. 3. (a) Band structure of the Hamiltonian (4) for $m = +1$ and $B = 2.0$ at $p_z = 0$. Only bands 2 and 3 are shown; the colors represent the value of the spin polarization (red: 1; blue: -1) along the z axis (parallel to $\vec{B}$). (b) The Berry phase $\theta(p_x)$ calculated for lines in the BZ from $p_z = -\pi$ to $p_z = \pi$.

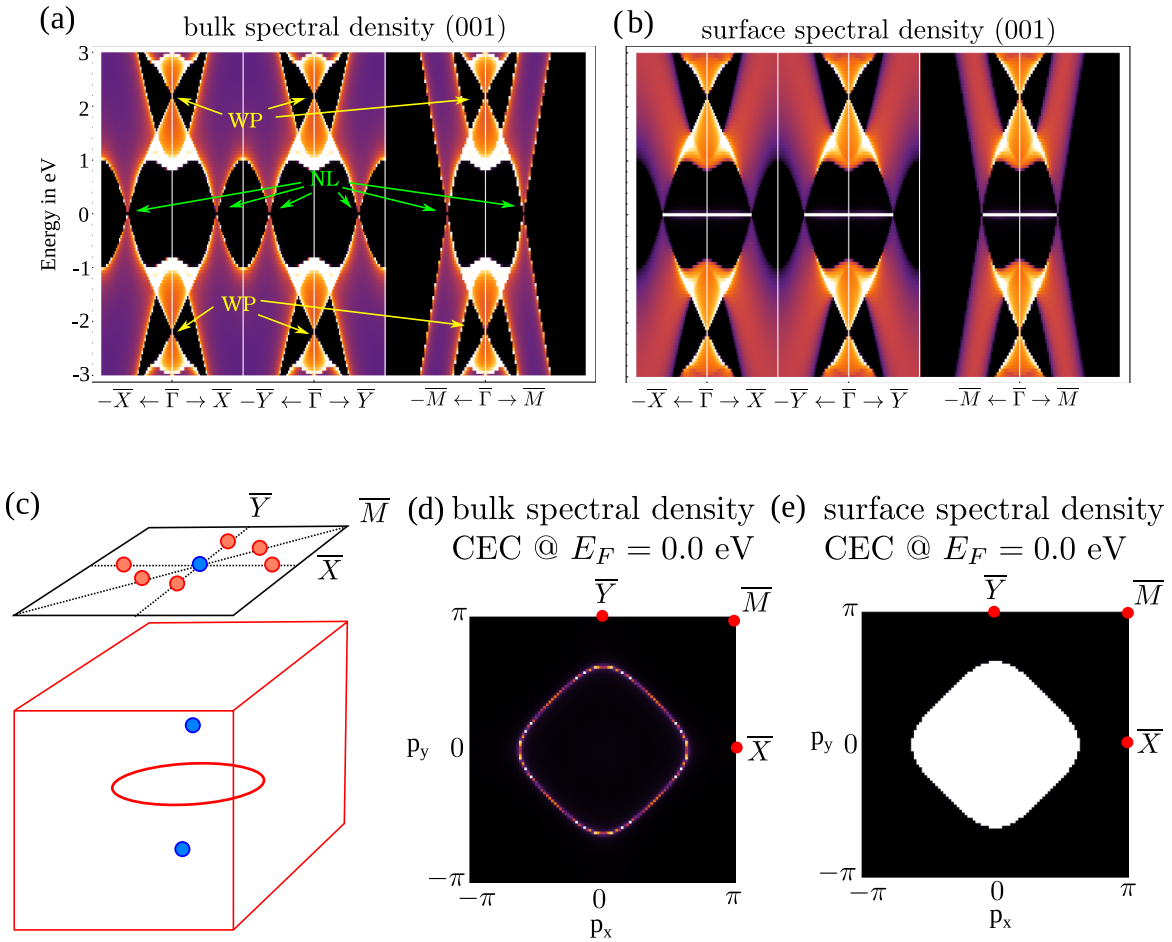

FIG. 4. Spectral density of the (001) surface represented as a color scale (black : low; white: high) for $m = +1$, $B = 2.0$. (a) Spectral density of the bulk layer along high-symmetry lines in the surface BZ; see (c). (b) Spectral density of the surface layer along high-symmetry lines in the surface BZ. (c) Bulk BZ (red) and (001) surface BZ (black) with the position of the band crossings and their projections onto the surface BZ, respectively (red: NL; blue: WPs). (d) Constant energy cut at $E_F = 0.0$ eV of the projected bulk layer. (e) Constant energy cut at $E_F = 0.0$ eV of the surface layer.

calculated along mirror-symmetric lines $\mathcal{L}$ in the BZ is quantized and takes on values of $\theta = 0, -\pi \mod 2\pi$. Effectively, $\vec{p} \in \mathcal{L}$ is a 1D subsystem possessing inversion symmetry, resulting from the mirror symmetry of the full system. The Berry phase of such a system is quantized, as shown by Zak [47]. In Appendix A we present an alternative way the Berry phase is quantized in the presence of mirror symmetry or particle-hole symmetry. The latter is a feature of the Hamiltonian (4) and is unlikely in real materials. It is $\theta(\mathcal{L}) = \pi \mod 2\pi$ if $\mathcal{L}$ and the NL are intertwined and $\theta(\mathcal{L}) = 0 \mod 2\pi$ otherwise (especially when there is no NL at all). As loop $\mathcal{L}$ we choose a line in the BZ parallel to p_z, going from $p_z = -\pi$ to $p_z = \pi$, i.e., from the bottom of the BZ to the top. Such a line $\mathcal{L}$ is closed by the periodic boundary conditions. Thus, for each $\vec{p}_\parallel = (p_x, p_y)$ the Berry phase $\theta(\vec{p}_\parallel)$ can be calculated and each step indicates crossing of the NL. For the calculation, we have rewritten Eq. (9) as a Wilson loop [48,49]

$$\theta(\mathcal{L}) = \sum_{n \in \text{occ.}} \operatorname{Im} \ln \prod_j \langle u_{n,\vec{p}_j} | u_{n,\vec{p}_j + \Delta\vec{p}} \rangle, \tag{10}$$

where $\vec{p}_j$ are points on a dense mesh on the line $\mathcal{L}$ and $\Delta\vec{p}$ is a distance between two adjacent points. The result of the calculation is shown in Fig. 3(b), where we plot the Berry phase $\theta(p_x)$ for $m = +1$ and $B = 2.0$. We obtain $\theta(p_x) = 0$ in the region where the line $\mathcal{L}$ does not pierce the NL and $\theta(p_x) = -\pi$ when $\mathcal{L}$ goes through the NL. Thus, we claim that the NL is protected by both the mirror symmetry and the nonzero Berry phase. Here we want to note that in Ref. [50] the authors discuss a NL in Ca_3P_2, which is protected by the same effects as the NL in this paper, i.e., the mirror symmetry and the Berry phase. The results of the corresponding Berry phase calculations for the double- and quadruple-NL phases are given in Appendix B.

C. Surface states

One of the most prominent features of all topological materials is the existence of surface states which are connected to the nontrivial topological features of the bulk bands. In WSMs, these are the *Fermi arcs*—surface states, which connect the surface projections of the WPs when cut at the energy of the WPs [51]. In the case of the NLSM, the corresponding surface state is called *drumhead surface state*, and it typically exists either inside or outside of the projection of the NL onto the surface [13,50].

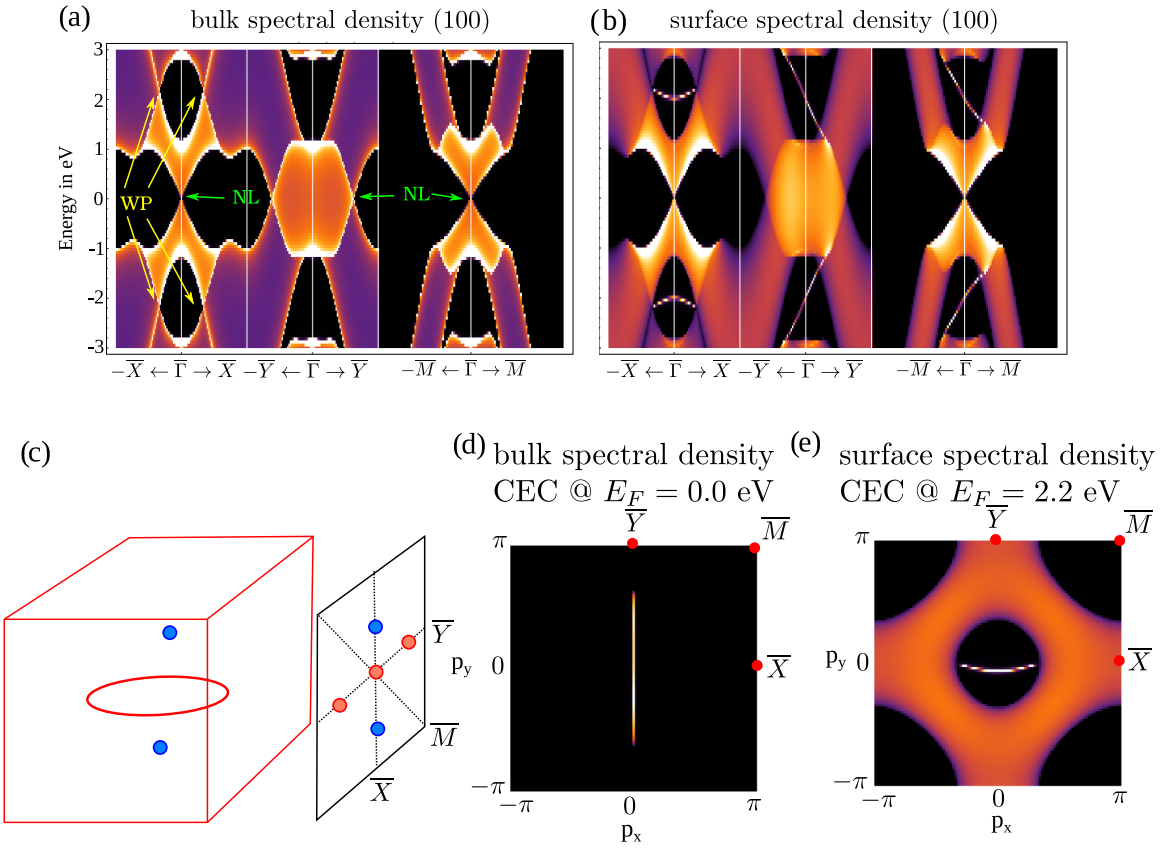

FIG. 5. Spectral density of the (100) surface represented as a color scale (black: low; white: high) for $m = +1$, $B = 2.0$. (a) Spectral density of the bulk layer along high-symmetry lines in the surface BZ; see (c). (b) Spectral density of the surface layer along high-symmetry lines in the surface BZ. (c) Bulk BZ (red) and (100) surface BZ (black) with the position of the band crossings and their projections onto the surface BZ, respectively (red: NL; blue: WPs). (d) Constant energy cut at $E_F = 0.0$ eV of the surface layer. (e) Constant energy cut at $E_F = 2.2$ eV of the surface layer.

In this work, we studied the surface electronic structure of the model in Eq. (4) by calculating the Green's function of the system in a layered semi-infinite geometry. Using the real-space formulation [Eq. (5)] enables one to decouple the inter- and intralayer parts. The layer-resolved Green's function $G_{\alpha,\alpha}(p_x, p_y)$ is calculated from a renormalization scheme described in Refs. [52,53]. The electronic structure is then given as the spectral density

$$N_l(E, p_x, p_y) = -\frac{1}{\pi} \operatorname{Im} \operatorname{Tr} G_{\alpha,\alpha}(E + i\eta, p_x, p_y) \qquad (11)$$

with the layer index α, and a small imaginary energy $\eta = 0.001$ eV. The results for $B = 2.0$ (single NL) are shown in Figs. 4 and 5 for the (001) surface (with a surface normal perpendicular to $\vec{B}$) and for the (100) surface (with a surface normal parallel to $\vec{B}$), respectively. Surface electronic structures of the multiple-NL phases are presented in Appendix B.

From Fig. 4(c) it becomes obvious that the WPs are both projected on the $\overline{\Gamma}$ point of the surface BZ (SBZ). These projected WPs can be seen in Figs. 4(a) and 4(b) at $E \approx \pm 2.2$ eV. The effective Chern number of the WP projection is $+1 + (-1) = 0$ and, hence, there are no Fermi arcs at the (001) surface. The projection of the NL, on the other hand, has exactly the same shape as the original bulk feature, as it is located in the $p_z = 0$ plane, parallel to the (001) SBZ. The crossings of the projected bulk bands can be observed in Figs. 4(a) and 4(b) along all considered high-symmetry lines $\overline{\Gamma}$-$\overline{X}$, $\overline{\Gamma}$-$\overline{Y}$, and $\overline{\Gamma}$-$\overline{M}$ at $E = 0.0$ eV. In the surface layer [Fig. 4(b)], the crossings are connected by a flat surface state. Its drumheadlike shape is visible in Fig. 4(e), as its surface spectral density is maximal inside the projected NL [Fig. 4(d)]. These findings are in line with the fact that there has to be a surface state either inside or outside of the NL projection onto the SBZ. The exact position of the surface state is not topologically protected by the Berry phase $\theta(p_x, p_y) = -\pi$ mod 2π, in contrast to its existence. The location of the surface state can depend on the surface termination [32]. Since the quantization of the Berry phase is given by mirror or particle-hole symmetry, the occurrence of the drumhead surface states may be viewed as being protected by these symmetries.

The situation on the (100) surface is demonstrated in Fig. 5(c). The WPs are projected on two different points along $-\overline{X}$-$\overline{\Gamma}$-$\overline{X}$, as can be seen in Figs. 5(a) and 5(b) at $E \approx \pm 2.2$ eV. Here, both WP projections are connected by a single surface state (Fermi arc), as is also shown for the constant energy cut (CEC) at $E \approx 2.2$ eV [Fig. 5(e)]. The projection of the NL is a single line along the $-\overline{Y}$-$\overline{\Gamma}$-$\overline{Y}$ direction in the (100) SBZ, which is demonstrated in the CEC at $E = 0.0$ eV [Fig. 5(d)].

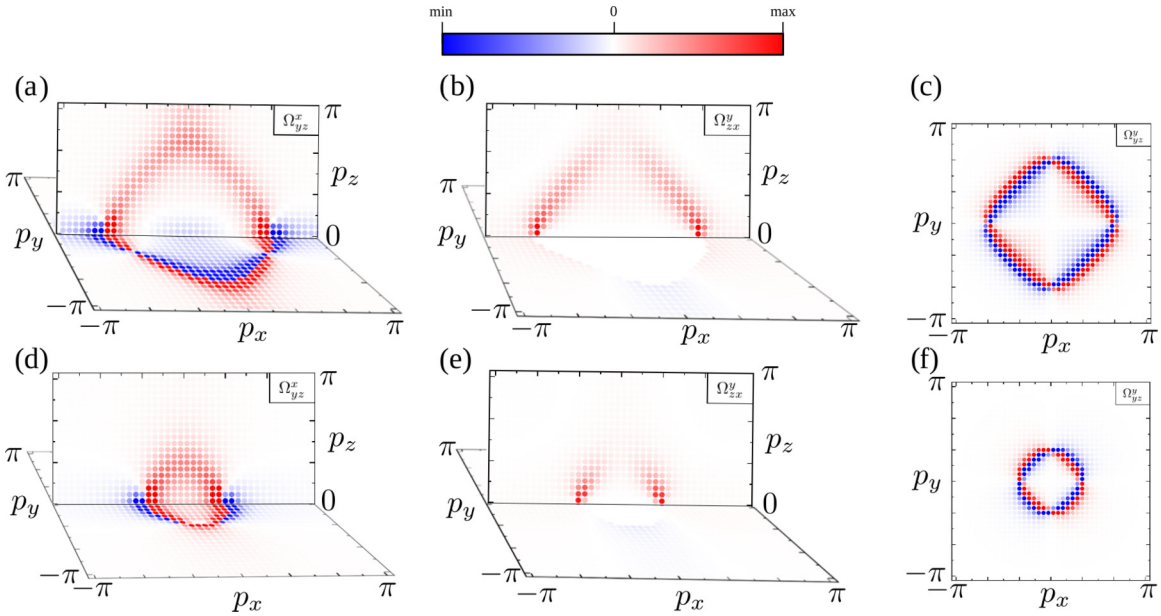

FIG. 6. Distribution of the spin Berry curvature $\Omega^l_{ij}(\vec{p}) = \sum_n \Omega^l_{n,ij}(\vec{p})$ summed over bands below $E = 0.0$ eV in the p_x-p_y and p_x-p_z planes, given as color scale, for systems with a NL ($B = 2.0$). Top: system with initial band inversion ($m = +1$). Bottom: system without a band inversion ($m = -1$). (a) and (d) Ω^x_{yz}. (b) and (e) Ω^y_{zx}. (c) and (f) Ω^y_{yz} (only the p_x-p_y plane is shown).

Overall, both the NL and the WPs possess characteristic surface states in the SBZ. The existence of these surface states and their shape depends strongly on the chosen surface, especially with respect to the magnetization direction.

III. ANOMALOUS AND SPIN HALL EFFECT

After having established that the system described by the model Hamiltonian (4) can harbor WPs and NLs, we will now show how these semimetallic features give rise to considerable AHC and SHC. These intrinsic phenomena are calculated from the linear-response Kubo formula [54–56]. For the AHC at $T = 0$ K we evaluated

$$\sigma_{ij} = -\frac{e^2}{\hbar} \sum_n \int_{BZ} \frac{d^3\vec{p}}{(2\pi)^3} \Omega_{n,ij}(\vec{p}), \tag{12}$$

with the Berry curvature

$$\Omega_{n,ij}(\vec{p}) = 2i\hbar^2 \sum_{m \neq n} \frac{\langle u_n(\vec{p})|\hat{v}_i|u_m(\vec{p})\rangle\langle u_m(\vec{p})|\hat{v}_j|u_n(\vec{p})\rangle}{[E_n(\vec{p}) - E_m(\vec{p})]^2} \tag{13}$$

of band n, which can be calculated from the eigenvalues $E_n(\vec{p})$ and the eigenvectors $|u_n(\vec{p})\rangle$ of the Hamiltonian $\hat{H}(\vec{p})$, as well as the velocity operator $\hat{v}_i = \frac{\partial \hat{H}}{\partial p_i}$, $i = x, y, z$. n is the band index and for zero temperature, only occupied bands contribute to the sum in Eq. (12). σ_{ij} describes the anomalous current density in direction i as a response to an electric field oriented in direction j.

The SHC can be calculated from

$$\sigma^l_{ij} = \frac{e}{\hbar} \sum_n \int_{BZ} \frac{d^3\vec{p}}{(2\pi)^3} \Omega^l_{n,ij}(\vec{p}), \tag{14}$$

where the integrand,

$$\Omega^l_{n,ij}(\vec{p}) = -2\,\mathrm{Im}\,\hbar^2 \sum_{m \neq n} \frac{\langle u_n(\vec{p})|\hat{j}^l_i|u_m(\vec{p})\rangle\langle u_m(\vec{p})|\hat{v}_j|u_n(\vec{p})\rangle}{[E_n(\vec{p}) - E_m(\vec{p})]^2}, \tag{15}$$

is sometimes called the spin Berry curvature. $\hat{j}^l_i$ is the spin current density operator in direction i with a spin orientation along l. The other quantities are as in Eq. (13). Also here, the spin current is driven by an electric field along direction j.

The model in Eq. (4) describes a simple cubic system for $\vec{B} = 0$. The finite exchange field along the z direction lowers the symmetry of the system, which then belongs to the tetragonal magnetic group $4/mm'm'$. According to Ref. [57], the AHC tensor of the studied Hamiltonian has only one independent nonzero off-diagonal element σ_{xy}. The situation becomes more complicated for the SHC tensor. In the nonmagnetic case (group $m\bar{3}m1'$), only the elements of σ^l_{ij} with $i \neq j \neq l \neq i$ can have nonzero values. The group $4/mm'm'$ allows also the elements σ^i_{iz}, $i = x, y$ and σ^z_{ii}, $i = x, y, z$ to be nonzero. For the former, we found numerically that the spin Berry curvature changes sign under a C_4 rotation along the p_z axis [see Figs. 6(c) and 6(f)]. Therefore, the total spin Berry curvature vanishes for these elements when integrated over the whole BZ. We did not calculate the diagonal elements of the SHC tensor.

To obtain numbers comparable with more realistic calculations, we chose for the interatomic distance $a = 3$ Å. The AHC and SHC are given in units of $(\Omega\,\mathrm{cm})^{-1}$ and $\frac{\hbar}{e}(\Omega\,\mathrm{cm})^{-1}$, respectively. The numerical integration over the BZ was performed on an equidistant mesh with 400^3 $\vec{p}$ points. For σ^x_{yz} we reach no convergence at $E = 0.0$ eV, i.e., exactly at the NL energy, and in its close vicinity, which we assign to the existence of the line singularity of the spin Berry curvature.

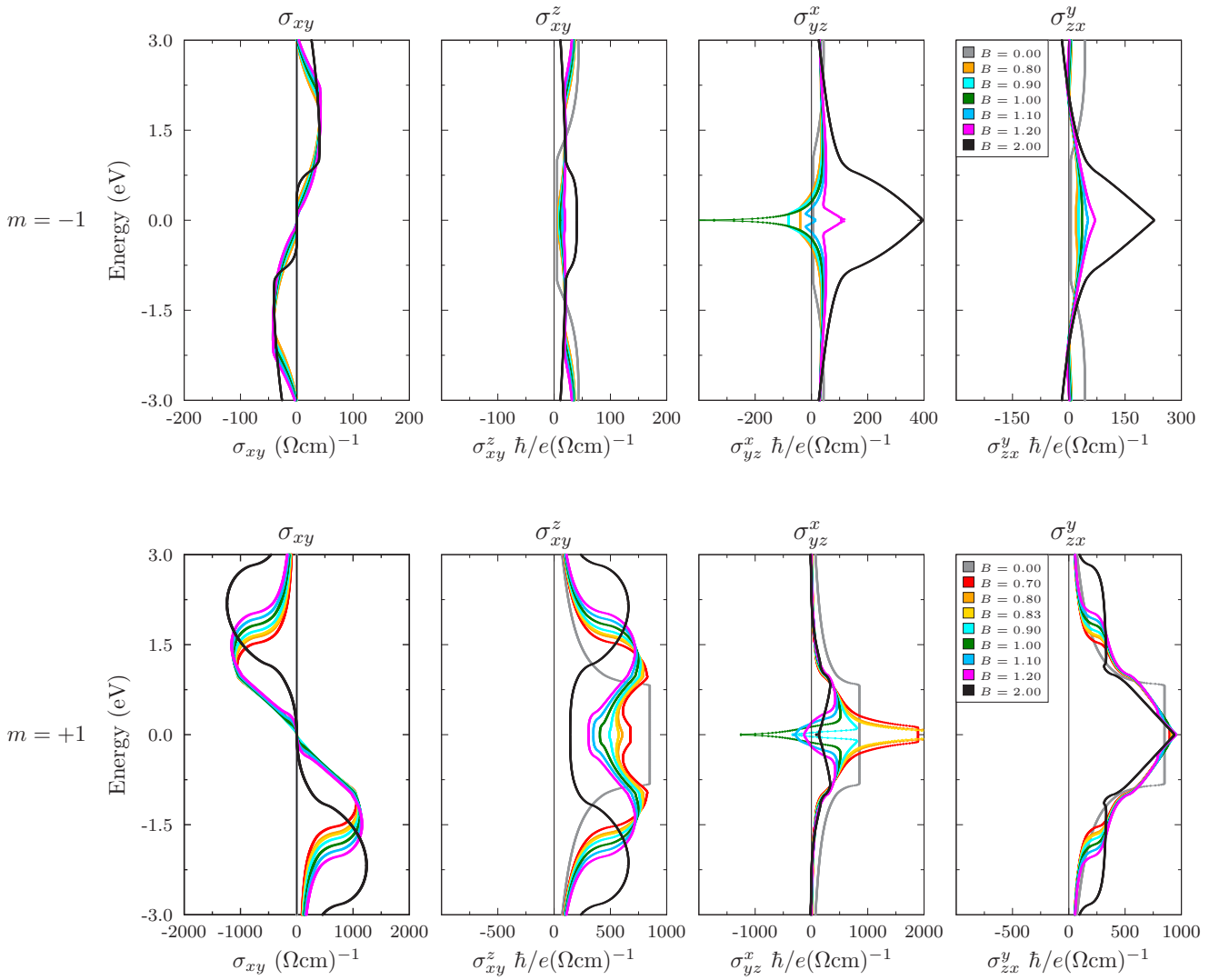

FIG. 7. Energy-dependent AHC and SHC for $m = -1$ (upper row) and $m = +1$ (lower row) for different exchange fields B (see color code in the panels for each row). Note the varying conductivity scale.

To perform the integration in this complicated situation, more sophisticated methods, such as adaptive meshes, have to be used. Therefore, the corresponding data points are not plotted.

In Fig. 7, we show the results of calculations of the AHC and SHC for $m = \pm 1$ and $B \in [0.0, 2.0]$ which can be compared with the band structures shown in Figs. 1 and 2. Only σ_{xy}, σ^z_{xy}, σ^x_{yz}, and σ^y_{zx} are shown, which are the only independent non-ero off-diagonal elements of the AHC and SHC tensors. In the following, we will discuss the influence of the topological features of the band structure on these transport properties.

(i) For the AHC σ_{xy} we find only small values for the trivial case ($m = -1$) which originate from the exchange field and SOC, intrinsically included in the Dirac equation. $\sigma_{xy} = 0$ for $B = 0$, because the Berry curvature vanishes in the presence of time-reversal and inversion symmetry. For $m = +1$, on the other hand, we observe large values of σ_{xy} for $B > 0$ with maxima located exactly at the WP energies (e.g., $E_{\max} = \pm 2.2\,\mathrm{eV}$ for $B = 2.0$). This effect of WPs inducing large values of the AHC was discussed previously [29,30] and it reflects the fact that the WPs are sources and sinks of the Berry curvature [43], a quantity which directly contributes to the AHC. Interestingly, the AHC shows no signatures of NLs in the band structure, for either $m = -1$ or $m = +1$.

(ii) The σ^z_{xy} component of the SHC tensor which describes the SHE in the x-y plane with spin polarization parallel to the exchange field shows behavior very similar to the AHC. For $m = -1$, again only moderate values were calculated, which originate from the presence of relativistic effects. For $m = +1$, we find large values originating from the WPs. When the spin polarization parallel to $\vec{B}$ can be assumed, then the relation between σ^z_{xy} and σ_{xy} is [31]

$$\sigma^z_{xy} = \pm \frac{\hbar}{2e} \sigma_{xy}. \tag{16}$$

As discussed in Ref. [30], the separation of the WPs along the p_z axis leads to large values of σ^z_{xy} and σ_{xy}. Since the system is a STI for $m = +1$ and $B = 0$, we also see a large constant value equal for all three components of the SHC tensor in the bulk band gap. A small exchange field breaks the cubic symmetry and the values of the three SHC elements

become different, but remain constant in the bulk band gap (for $B < 0.8165$). The system is no longer a STI, because the exchange field breaks the time-reversal symmetry, but it can still be characterized by other nontrivial topological invariants, such as the mirror Chern number (cf. Ref. [58]). σ_{xy}^{z} becomes smaller upon increasing the exchange field. As for the AHC, there is no significant effect of the NLs on the SHC.

(iii) The σ_{yz}^{x} component of the SHC tensor shows the most interesting behavior. First, the corresponding spin Berry curvature obtains large positive and negative values when the energy difference between the bands becomes small, especially in the regions of the band inversion "camel back" and at the NLs [see Figs. 6(a) and 6(d)]. For $m = -1$, σ_{yz}^{x} increases in the vicinity of $E = 0.0\,\mathrm{eV}$ with a stronger exchange field B. For $B = 1.0$ the SHC obtains a large negative value as the band gap closes at Γ. For larger values of B there is a NL in the band structure, which means the conduction band becomes a valence band inside the NL, and vice versa. Both bands carry spin Berry curvature of the same magnitude but of opposite sign. Therefore, after the band order changes, the SHC immediately obtains positive values at $E = 0.0\,\mathrm{eV}$ originating from the band inversion causing the NL to exist. Even larger exchange fields enhance this effect and the SHC can obtain values comparable with those of diamond and zinc-blende semiconductors with considerable SOC [59].

The situation is similar for $m = +1$. In addition to the previous case, the initial band inversion leads to a plateau of σ_{yz}^{x} in the band gap for $B < B_c^1$. As B increases, the SHC obtains large positive values [several thousand], since the spin Berry curvature of the topmost valence band becomes also large positive near the band inversion region. Like for $m = -1$, the existence of the NLs leads to a band inversion of bands with opposite spin Berry curvature. This, in turn, causes σ_{yz}^{x} to obtain a negative contribution near $E = 0.0\,\mathrm{eV}$ in addition to the positive offset originating from the initial band inversion. Note that overall the SHC for $m = +1$ is an order of magnitude larger than for $m = -1$. These values are comparable with those calculated for Au or Pd [54].

(iv) Finally, we obtain moderate values also for σ_{zx}^{y}. Figures 6(b) and 6(e) illustrate that for both $m = \pm 1$ the spin Berry curvature is large when the energy difference between valence and conduction bands is small, but there is no significant direct influence of the NLs on the SHC. Thus, for $m = -1$ values similar to σ_{yz}^{x} are calculated, originating from the band inversion connected with the existence of the NL. Similarly, for $m = +1$ the largest effect is the presence of the initial band inversion in the band structure. Increasing the exchange field and closing the band gap does not lead to an enhancement of the SHC. In addition, σ_{zx}^{y} is sensitive to the existence of WPs in the band structure, but the SHC values are smaller than for σ_{xy}^{z}.

Overall, the AHC σ_{xy} and the components of the SHC tensor show a very different response to the existence of topological nodal objects in the band structure. σ_{xy} and σ_{xy}^{z} (external electric field and spin current in the x-y plane, perpendicular to the exchange field) are large in the vicinity of WPs. In contrast, σ_{yz}^{x} (external electric field parallel to the exchange field, spin current, and the spin polarization perpendicular to it) becomes large near the NL energy. In addition, it can even change the sign at the phase transition between an insulating and NLSM phase. This effect could be used to switch the direction of the spin current upon increasing or decreasing the exchange field. Finally, σ_{zx}^{y} (spin current along the direction of the exchange field driven by an electric field perpendicular to it) is mostly influenced by the existence of an avoided or a real crossing between bands. The NL shows no enhancement of this component and the effect of the WPs is smaller than for σ_{xy}^{z}.

IV. REALISTIC MATERIALS

After having established that ferromagnetic order can lead to NLs and WPs (in the presence of an initial band inversion) in the bulk band structure, which themselves can cause the AHE and SHE to reach considerably large values, we discuss realizations of this situation in realistic materials. To the best of our knowledge, there are three theoretical predictions of ferromagnetic materials possessing a NL: $HgCr_2Se_4$ [34] and Co_2TiX ($X =$ Se, Ge, or Sn) [36] feature a NL in the p_x-p_y plane protected by the mirror symmetry of this plane, accompanied by a pair of WPs along p_z, i.e., parallel to the magnetization direction. These features fit to those in our model. Another ferromagnetic material, CrO_2 [35], was predicted to possess NLs on the faces of its fcc BZ. These NLs do not directly correspond to our findings, yet their origin—mirror planes in the BZ perpendicular to the magnetization—are the same.

In addition to these known materials, we predict here a way to systematically create ferromagnetic NLSMs from narrow-gap semiconductors. The initial semiconductor can, but does not have to be topologically nontrivial. Doping the semiconductor with magnetic atoms could lead to a finite magnetization, which has to be large enough to ensure that the exchange splitting of valence and conduction bands is of the order of the band gap. The second condition for a NL to occur is the same magnetization direction of atoms contributing to valence and conduction bands. Otherwise, bands with the same mirror eigenvalues would overlap, which leads to avoided crossings, rather than a NL. This happens, for example, in Cr-doped STI Sb_2Te_3 [60], where the magnetizations of Sb and Te are antiparallel, which contribute to the valence and conduction band at Γ, respectively. If the induced magnetization would be strong enough to bridge the insulating band gap, no NL would appear. Nevertheless, the combination of a magnetization and a band inversion should give rise to WPs at the band edges as described by our model. These WPs should lead to considerable values of AHC and SHC perpendicular to the magnetization.

V. CONCLUSION

In this work, we studied ferromagnetic topological semimetals featuring WPs and NLs, exploiting a lattice model based on the extended Dirac equation. Our recipe to realize ferromagnetic WSMs and NLSMs is to begin with a topologically trivial or nontrivial insulator and sufficiently increase the exchange field. We show that this procedure can lead to WPs and NLs as proven by calculating the bulk topological invariants and observing typical surface states (Fermi arcs and drumhead surface states) in the surface electronic structure of

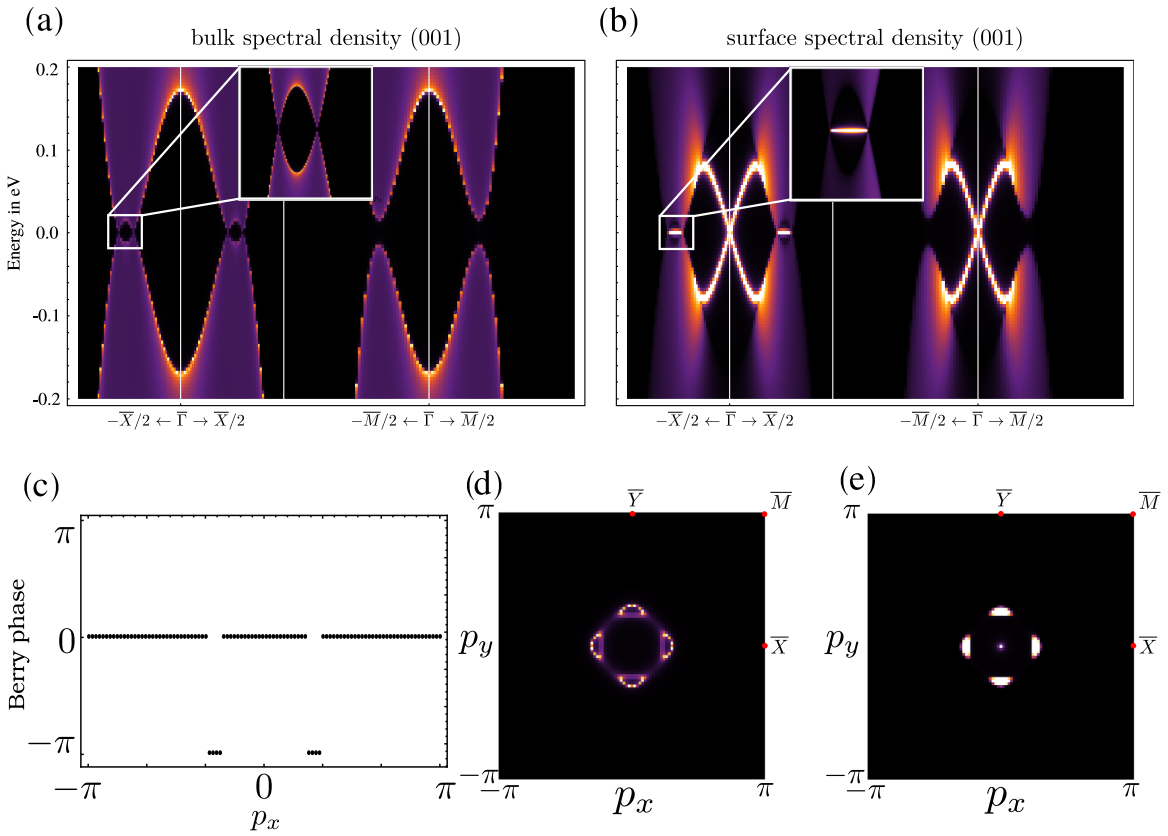

FIG. 8. Spectral density of the (001) surface represented as a color scale (black: low; white: high) for $m = +1$, $B = 0.83$. (a) Spectral density of the bulk layer along high-symmetry lines in the surface BZ. (b) Spectral density of the surface layer along high-symmetry lines in the surface BZ. (c) The Berry phase $\theta(p_x)$ calculated for lines in the BZ from $p_z = -\pi$ to $p_z = \pi$. (d) Constant energy cut at $E_F = 0.0$ eV of the bulk layer. (e) Constant energy cut at $E_F = 0.0$ eV of the surface layer.

various surfaces. Furthermore, we show that intrinsic AHC and SHC are strongly enhanced by the presence of WPs and NLs in the bulk band structure. Of particular importance is the fact that also spin currents with spin polarization perpendicular to the magnetization can gain considerable values.

In addition to ferromagnetic semimetals, the existence of WPs and NLs has been recently studied also in antiferromagnets with collinear (e.g., Refs. [61,62]) and noncollinear (e.g., Refs. [38,63]) magnetic structure, also leading to large conductivities. In order to study these and other topological semimetals, various extensions of the model Hamiltonian (4) are conceivable. To break the particle-hole symmetry present in our model, a term $\propto p^2$ can be added. This would, for example, lead to a modification of the dispersion along the nodal line, which is perfectly flat in energy without this extension. Another way to modulate the NL and WPs and test their stability is to tilt the direction of the exchange field. Within the present tight-binding formulation it is straightforward to investigate various collinear and noncollinear magnetic configurations. Finally, defining complex hopping parameters resulting from the Peierls substitution can be used to study Landau levels in magnetic topological semimetals.

ACKNOWLEDGMENT

This work was supported by the Priority Program SPP 1666 of Deutsche Forschungsgemeinschaft (DFG).

APPENDIX A: QUANTIZATION OF THE BERRY PHASE

Here we show the quantization of the Berry phase in the presence of mirror or particle-hole symmetry. Our derivation is similar to that in the Appendix of Ref. [64].

The Berry phase γ_n of band n along a line $\mathcal{L}$ connecting the boundaries of the Brillouin zone is given by

$$\gamma_n = i \int_{-\pi}^{\pi} \langle u_n(\vec{p}) | \nabla_{\vec{p}}\, u_n(\vec{p}) \rangle d\vec{p}.$$

The integrand

$$A_n(\vec{p}) = i \langle u_n(\vec{p}) | \nabla_{\vec{p}}\, u_n(\vec{p}) \rangle$$

is the Berry connection. For simplicity we assume that the band n is isolated along $\mathcal{L}$.

1. Quantization by mirror symmetry

We assume that the Hamiltonian $\hat{H}$ of the system is mirror symmetric with respect to the xy plane and the line $\mathcal{L}$ is perpendicular to the mirror plane in the Brillouin zone. The problem then becomes one dimensional, allowing one to fix p_x and p_y. We thus have

$$\hat{M}\hat{H}(p_z) = \hat{H}(-p_z)\hat{M},$$

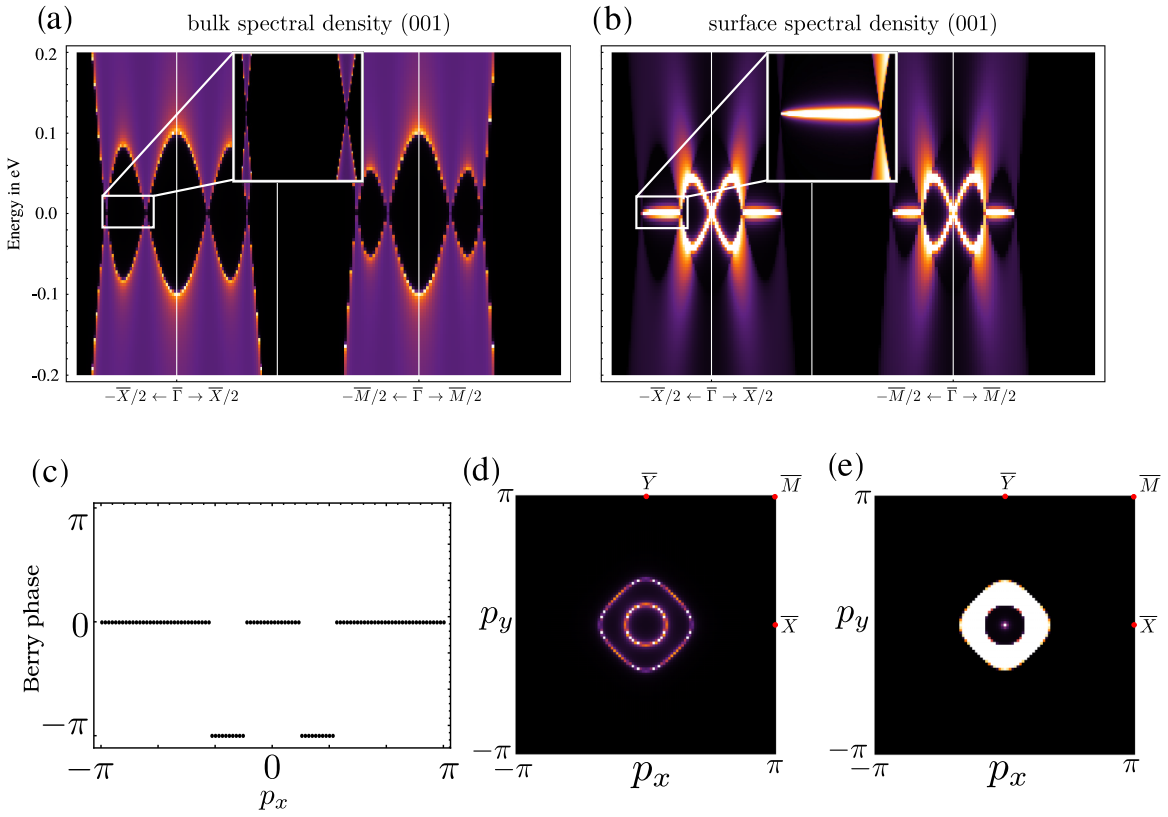

FIG. 9. Spectral density of the (001) surface represented as a color scale (black: low; white: high) for $m = +1$, $B = 0.90$. (a) Spectral density of the bulk layer along high-symmetry lines in the surface BZ. (b) Spectral density of the surface layer along high-symmetry lines in the surface BZ. (c) The Berry phase $\theta(p_x)$ calculated for lines in the BZ from $p_z = -\pi$ to $p_z = \pi$. (d) Constant energy cut at $E_F = 0.0$ eV of the bulk layer. (e) Constant energy cut at $E_F = 0.0$ eV of the surface layer.

with the reflection operator $\hat{M}$. Starting from the stationary Schrödinger equation

$$\hat{H}(p_z)|u_n(p_z)\rangle = E_n(p_z)|u_n(p_z)\rangle$$

we obtain

$$\hat{M}\hat{H}(p_z)|u_n(p_z)\rangle = E_n(p_z)\hat{M}|u_n(p_z)\rangle,$$
$$\hat{H}(-p_z)\hat{M}|u_n(p_z)\rangle = E_n(p_z)\hat{M}|u_n(p_z)\rangle,$$

and by replacing $p_z \leftrightarrow -p_z$

$$\hat{H}(p_z)\hat{M}|u_n(-p_z)\rangle = E_n(-p_z)\hat{M}|u_n(-p_z)\rangle.$$

Comparison with the Schrödinger equation gives

$$E_n(p_z) = E_n(-p_z), \tag{A1a}$$
$$|u_n(p_z)\rangle = e^{i\varphi(p_z)}\hat{M}|u_n(-p_z)\rangle, \tag{A1b}$$

with some phase factor $\exp[i\varphi(p_z)]$. With this, the Berry connection becomes

$$\begin{aligned} A_n(p_z) &= i\langle u_n(\vec{p})|\nabla_{\vec{p}}u_n(\vec{p})\rangle \\ &= i\langle u_n(-p_z)|\hat{M}^\dagger e^{-i\varphi(p_z)}\partial_{p_z}e^{i\varphi(p_z)}\hat{M}|u_n(-p_z)\rangle \\ &= -\partial_{p_z}\varphi(p_z) - A_n(-p_z) \end{aligned}$$

and the Berry phase reads

$$\begin{aligned} \gamma_n &= \int_{-\pi}^{\pi} A_n(p_z)dp_z \\ &= -\int_{-\pi}^{\pi} \partial_{p_z}\varphi(p_z)dp_z - \int_{-\pi}^{\pi} A_n(-p_z)dp_z \\ &= -\varphi|_{-\pi}^{\pi} - \int_{-\pi}^{\pi} A_n(-p_z)dp_z \\ &= 2\pi m - \gamma_n, \end{aligned}$$

with m integer. Thus, we obtain a quantized Berry curvature $\gamma_n = \pi m$. Since the Berry phase is defined modulo 2π, γ_n can only take values of 0 or π. The same then holds also for the total Berry phase summed over all occupied bands.

2. Quantization by particle-hole symmetry

We now assume that the Hamiltonian $\hat{H}$ has particle-hole symmetry and the isolated band n is occupied. Considering the line $\mathcal{L}$ in the Brillouin zone as before, we have

$$\hat{C}\hat{H}(p_z) = -\hat{H}(-p_z)\hat{C},$$

with the charge conjugation operator $\hat{C}$. As for the mirror symmetry it follows for band n

$$\hat{H}(p_z)|u_n(p_z)\rangle = E_n(p_z)|u_n(p_z)\rangle,$$
$$\hat{C}\hat{H}(p_z)|u_n(p_z)\rangle = E_n(p_z)\hat{C}|u_n(p_z)\rangle,$$

$$-\hat{H}(-p_z)\hat{C}|u_n(p_z)\rangle = E_n(p_z)\hat{C}|u_n(p_z)\rangle,$$
$$\hat{H}(-p_z)\hat{C}|u_n(p_z)\rangle = -E_n(p_z)\hat{C}|u_n(p_z)\rangle,$$
$$\hat{H}(p_z)\hat{C}|u_n(-p_z)\rangle = -E_n(-p_z)\hat{C}|u_n(-p_z)\rangle,$$

and

$$E_n(p_z) = -E_n(-p_z), \tag{A2a}$$
$$|u_n(p_z)\rangle = e^{i\varphi(p_z)}\hat{C}|u_n(-p_z)\rangle. \tag{A2b}$$

The last equation has the same form as the corresponding one for the mirror symmetry, Eq. (A1), with the exception that $|u_n(-p_z)\rangle$ is an unoccupied state. We rename the band index $n \to \tilde{n} = N + 1 - n$ with the total number of bands N on the right-hand side of the last equation to make clear that $|u_{\tilde{n}}(-p_z)\rangle$ belongs to a different band than $|u_n(p_z)\rangle$. This leads to $\gamma_n = 2\pi m + \gamma_{\tilde{n}}$ with $\tilde{n}$ denoting the unoccupied band. Since the sum of the Berry phases of all bands vanishes, we can use $\gamma_n = -\gamma_{\tilde{n}}$ to obtain the quantization $\gamma_n = \pi m$, m integer, in the presence of particle-hole symmetry.

APPENDIX B: PHASES WITH MULTIPLE NODAL LINES

In Fig. 8 we show the projected bulk and surface electronic structure for the (001) termination for $B = 0.83$. Four NLs can be identified crossing the Γ-X line in the BZ. The Berry phase of a line along p_z in the bulk BZ is 0 when it does not pierce the NLs and its value is $-\pi$ otherwise [Fig. 8(c)].

We obtain a similar result for $B = 0.90$ shown in Fig. 9. In this case, there is a pair of NLs which harbor a drumhead surface state between them at the (001) surface. The calculation of the Berry phase again confirms the nontrivial topological character of the NL.

Finally, for both $B = 0.83$ and $B = 0.90$ we observe a surface state at $\overline{\Gamma}$ in addition to the drumhead surface state. This surface state is left over from the topological surface state connected with the STI character of the system with vanishing exchange field.

[1] B. A. Bernevig, T. L. Hughes, and S.-C. Zhang, Science **314**, 1757 (2006).
[2] M. König, S. Wiedmann, C. Brüne, A. Roth, H. Buhmann, L. W. Molenkamp, X.-L. Qi, and S.-C. Zhang, Science **318**, 766 (2007).
[3] M. Z. Hasan and C. Kane, Rev. Mod. Phys. **82**, 3045 (2010).
[4] S. M. Young, S. Zaheer, J. C. Y. Teo, C. L. Kane, E. J. Mele, and A. M. Rappe, Phys. Rev. Lett. **108**, 140405 (2012).
[5] Z. Wang, Y. Sun, X.-Q. Chen, C. Franchini, G. Xu, H. Weng, X. Dai, and Z. Fang, Phys. Rev. B **85**, 195320 (2012).
[6] Z. Wang, H. Weng, Q. Wu, X. Dai, and Z. Fang, Phys. Rev. B **88**, 125427 (2013).
[7] J. A. Steinberg, S. M. Young, S. Zaheer, C. L. Kane, E. J. Mele, and A. M. Rappe, Phys. Rev. Lett. **112**, 036403 (2014).
[8] B.-J. Yang and N. Nagaosa, Nat. Commun. **5**, 4898 (2014).
[9] B. Q. Lv, H. M. Weng, B. B. Fu, X. P. Wang, H. Miao, J. Ma, P. Richard, X. C. Huang, L. X. Zhao, G. F. Chen, Z. Fang, X. Dai, T. Qian, and H. Ding, Phys. Rev. X **5**, 031013 (2015).
[10] S.-Y. Xu, I. Belopolski, N. Alidoust, M. Neupane, G. Bian, C. Zhang, R. Sankar, G. Chang, Z. Yuan, C.-C. Lee, S.-M. Huang, H. Zheng, D. S. Sanchez, B. Wang, A. Bansil, F. Chou, P. P. Shibayev, H. Lin, S. Jia, and M. Z. Hasan, Science **349**, 613 (2015).
[11] L. X. Yang, Z. K. Liu, Y. Sun, H. Peng, H. F. Yang, T. Zhang, B. Zhou, Y. Zhang, Y. F. Guo, M. Rahn, D. Prabhakaran, Z. Hussain, S.-K. Mo, C. Felser, B. Yan, and Y. L. Chen, Nat. Phys. **11**, 728 (2015).
[12] B. Yan and C. Felser, Annu. Rev. Condens. Matter Phys. 337 **8** (2017).
[13] A. A. Burkov, M. D. Hook, and L. Balents, Phys. Rev. B **84**, 235126 (2011).
[14] R. Yu, H. Weng, Z. Fang, X. Dai, and X. Hu, Phys. Rev. Lett. **115**, 036807 (2015).
[15] J. Zhao, R. Yu, H. Weng, and Z. Fang, Phys. Rev. B **94**, 195104 (2016).
[16] G. Bian, T.-R. Chang, R. Sankar, S.-Y. Xu, H. Zheng, T. Neupert, C.-K. Chiu, S.-M. Huang, G. Chang, I. Belopolski, D. S. Sanchez, M. Neupane, N. Alidoust, C. Liu, B. Wang, C.-C. Lee, H.-T. Jeng, C. Zhang, Z. Yuan, S. Jia, A. Bansil, F. Chou, H. Lin, and M. Z. Hasan, Nat. Commun. **7**, 10556 (2016).
[17] Q. Xu, R. Yu, Z. Fang, X. Dai, and H. Weng, Phys. Rev. B **95**, 045136 (2017).
[18] R. Yu, Q. Wu, Z. Fang, and H. Weng, Phys. Rev. Lett. **119**, 036401 (2017).
[19] B. Bradlyn, J. Cano, Z. Wang, M. G. Vergniory, C. Felser, R. J. Cava, and B. A. Bernevig, Science **353**, 558 (2016).
[20] R. Yu, W. Zhang, H.-j. Zhang, S.-C. Zhang, X. Dai, and Z. Fang, Science **329**, 61 (2010).
[21] C.-Z. Chang, J. Zhang, X. Feng, J. Shen, Z. Zhang, M. Guo, K. Li, Y. Ou, P. Wei, L.-L. Wang, Z.-Q. Ji, Y. Feng, S. Ji, X. Chen, J. Jia, X. Dai, Z. Fang, S.-C. Zhang, K. He, Y. Wang, L. Lu, X.-C. Ma, and Q.-K. Xue, Science **340**, 167 (2013).
[22] C. L. Kane and E. J. Mele, Phys. Rev. Lett. **95**, 146802 (2005).
[23] C. L. Kane and E. J. Mele, Phys. Rev. Lett. **95**, 226801 (2005).
[24] B. A. Bernevig and S.-C. Zhang, Phys. Rev. Lett. **96**, 106802 (2006).
[25] S. Murakami, N. Nagaosa, and S.-C. Zhang, Science **301**, 1348 (2003).
[26] J. Sinova, D. Culcer, Q. Niu, N. A. Sinitsyn, T. Jungwirth, and A. H. MacDonald, Phys. Rev. Lett. **92**, 126603 (2004).
[27] L. Matthes, S. Küfner, J. Furthmüller, and F. Bechstedt, Phys. Rev. B **94**, 085410 (2016).
[28] H. B. Nielsen and M. Ninomiya, Phys. Lett. B **130**, 389 (1983).
[29] A. A. Burkov, Phys. Rev. Lett. **113**, 187202 (2014).
[30] K. Y. Yang, Y. M. Lu, and Y. Ran, Phys. Rev. B **84**, 075129 (2011).
[31] Y. Sun, Y. Zhang, C. Felser, and B. Yan, Phys. Rev. Lett. **117**, 146403 (2016).
[32] M. Hirayama, R. Okugawa, T. Miyake, and S. Murakami, Nat. Commun. **8**, 14022 (2017).

[33] G. Bian, T. R. Chang, H. Zheng, S. Velury, S. Y. Xu, T. Neupert, C. K. Chiu, S. M. Huang, D. S. Sanchez, I. Belopolski, N. Alidoust, P. J. Chen, G. Chang, A. Bansil, H. T. Jeng, H. Lin, and M. Z. Hasan, Phys. Rev. B **93**, 121113(R) (2016).
[34] G. Xu, H. Weng, Z. Wang, X. Dai, and Z. Fang, Phys. Rev. Lett. **107**, 186806 (2011).
[35] R. Wang, J. Z. Zhao, Y. J. Jin, Y. P. Du, Y. X. Zhao, H. Xu, and S. Y. Tong, arXiv:1705.07076.
[36] G. Chang, S.-Y. Xu, H. Zheng, B. Singh, C.-H. Hsu, G. Bian, N. Alidoust, I. Belopolski, D. S. Sanchez, S. Zhang, H. Lin, and M. Z. Hasan, Sci. Rep. **6**, 38839 (2016).
[37] S.-Q. Shen, W.-Y. Shan, and H.-Z. Lu, Spin **01**, 33 (2011).
[38] Y. Zhang, Y. Sun, H. Yang, J. Železný, S. P. P. Parkin, C. Felser, and B. Yan, Phys. Rev. B **95**, 075128 (2017).
[39] J. Yu, B. Yan, and C.-X. Liu, Phys. Rev. B **95**, 235158 (2017).
[40] P. Dirac, Proc. R. Soc. A **778**, 610 (1928).
[41] K.-I. Imura, A. Yamakage, S. Mao, A. Hotta, and Y. Kuramoto, Phys. Rev. B **82**, 085118 (2010).
[42] D. J. Thouless, M. Kohmoto, M. P. Nightingale, and M. den Nijs, Phys. Rev. Lett. **49**, 405 (1982).
[43] M. Berry, Proc. R. Soc. London, Ser. A **392**, 45 (1984).
[44] S. Murakami, New J. Phys. **9**, 356 (2007).
[45] D. Xiao, M.-C. Chang, and Q. Niu, Rev. Mod. Phys. **82**, 1959 (2010).
[46] H. Huang, J. Liu, D. Vanderbilt, and W. Duan, Phys. Rev. B **93**, 201114(R) (2016).
[47] J. Zak, Phys. Rev. Lett. **62**, 2747 (1989).
[48] R. D. King-Smith and D. Vanderbilt, Phys. Rev. B **47**, 1651 (1993).
[49] R. Yu, X. L. Qi, A. Bernevig, Z. Fang, and X. Dai, Phys. Rev. B **84**, 075119 (2011).
[50] Y.-H. Chan, C.-K. Chiu, M. Y. Chou, and A. P. Schnyder, Phys. Rev. B **93**, 205132 (2016).
[51] X. Wan, A. M. Turner, A. Vishwanath, and S. Y. Savrasov, Phys. Rev. B **83**, 205101 (2011).
[52] A. Bödicker, W. Schattke, J. Henk, and R. Feder, J. Phys.: Condens. Matter **6**, 1927 (1994).
[53] J. Henk and W. Schattke, Comput. Phys. Commun. **77**, 69 (1993).
[54] G. Y. Guo, J. Appl. Phys. **105**, 07C701 (2009).
[55] M. Gradhand, D. V. Fedorov, F. Pientka, P. Zahn, I. Mertig, and B. L. Györffy, J. Phys.: Condens. Matter **24**, 213202 (2012).
[56] J. Sinova, S. O. Valenzuela, J. Wunderlich, C. H. Back, and T. Jungwirth, Rev. Mod. Phys. **87**, 1213 (2015).
[57] M. Seemann, D. Ködderitzsch, S. Wimmer, and H. Ebert, Phys. Rev. B **92**, 155138 (2015).
[58] T. Rauch, M. Flieger, J. Henk, I. Mertig, and A. Ernst, Phys. Rev. Lett. **112**, 016802 (2014).
[59] G. Y. Guo, Y. Yao, and Q. Niu, Phys. Rev. Lett. **94**, 226601 (2005).
[60] M. G. Vergniory, M. M. Otrokov, D. Thonig, M. Hoffmann, I. V. Maznichenko, M. Geilhufe, X. Zubizarreta, S. Ostanin, A. Marmodoro, J. Henk, W. Hergert, I. Mertig, E. V. Chulkov, and A. Ernst, Phys. Rev. B **89**, 165202 (2014).
[61] L. Šmejkal, J. Železný, J. Sinova, and T. Jungwirth, Phys. Rev. Lett. **118**, 106402 (2017).
[62] W. Brzezicki and M. Cuoco, Phys. Rev. B **95**, 155108 (2017).
[63] H. Yang, Y. Sun, Y. Zhang, W.-J. Shi, S. S. P. Parkin, and B. Yan, New J. Phys. **19**, 015008 (2017).
[64] A. Lau, J. van den Brink, and C. Ortix, Phys. Rev. B **94**, 165164 (2016).